J. Fluid Mech. (1969), *vol.* 38, *part* 2, *pp.* 255–271
Printed in Great Britain

A laboratory model of the wind-driven ocean circulation

By R. C. BEARDSLEY
Meteorology Department, Massachusetts Institute of Technology

(Received 24 June 1968 and in revised form 25 March 1969)

A simple laboratory model for the wind-driven ocean circulation is re-studied experimentally and theoretically. Introduced by Pedlosky & Greenspan (1967), the model consists of a rotating cylinder with sloping bottom, the fluid inside being driven by the steady relative rotation of the cylinder's lid. A linear theory is developed to illustrate the modification in the interior and Stewartson boundary layers caused by variation of the bottom slope from 0 to $O(1)$; Stommel's (1948) model is obtained when the bottom slope $\tan\alpha \ll E^{\frac{1}{4}}$, and the Munk & Carrier (1950) model is obtained for $E^{\frac{1}{4}} \ll \tan\alpha \ll 1$ (E is the Ekman number). Measurements of the interior cross-contour 'Sverdrup' velocity agree well with theory when the Ekman-layer Reynolds number R_E is ≈ 1 or less. The western boundary-layer azimuthal velocity agrees reasonably well with theory, although the observed variation with depth and bottom slope were not predicted. The western boundary layer shows downstream intensification when R_E is increased from ≈ 1 until topographic Rossby waves appear in the transition region between western boundary layer and interior. The motion becomes unstable when a critical value of R_E is reached, independent of the bottom slope, and a low-frequency two-dimensional flow oscillation is observed. A brief comparison is made with previous wind-driven ocean circulation studies.

1. Introduction

We consider here the slow, viscously driven motion of an incompressible homogeneous fluid in a rapidly rotating cylinder with sloping bottom. The configuration (shown in figure 1) is called a 'sliced cylinder', since the lower surface is formed by a plane intersecting the cylinder at an angle α. The upper surface is normal to the cylinder axis and rotates steadily with an angular velocity $(1+\epsilon)\,\Omega$, while the rest of the container rotates at Ω.

Pedlosky & Greenspan (1967) introduced this model to demonstrate the modifications of Greenspan's (1965) general theory for flow in a rotating fluid container with open geostrophic contours. They also noted the similarity of the model flow to the large-scale ocean circulation. The physical analogy between vortex stretching by motion across bottom contours, and the creation of relative vorticity by the northward increase in horizontal Coriolis acceleration (the β-effect), enables the sliced cylinder to model several important features of the theoretical wind-driven ocean circulation problem.

To exploit this analogy, however, and draw oceanographic inferences, we

must first thoroughly understand the laboratory model itself. Pedlosky & Greenspan show that the symmetric character of the flow obtained for zero bottom slope changes completely when the depth variation exceeds the scaled Ekman-layer thickness. The interior dynamics remain geostrophic, but the finite

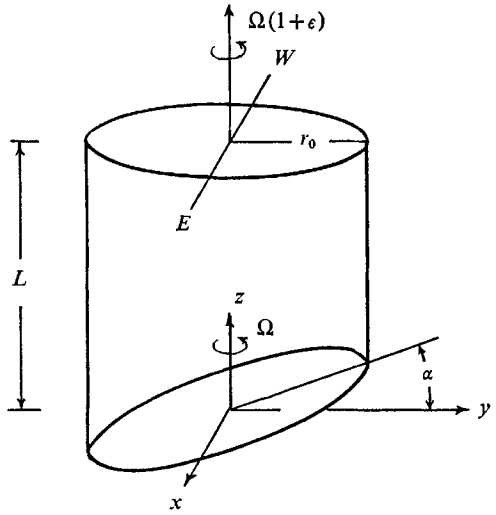

FIGURE 1

bottom slope constrains the flow to a slow drift across the depth contours, and the horizontal circulation is closed by a strong viscous boundary current along the western side wall. A series of preliminary experiments by the author qualitatively confirmed these results, but also showed several features which could not be explained (see Pedlosky & Greenspan).

Presented in this paper is a re-examination of the sliced cylinder model. The linear analysis of Pedlosky & Greenspan is extended in §2 to cover a wider range of bottom slopes, in order to clarify the physical mechanisms underlying several types of western boundary layers. This will also show under what conditions the laboratory model is analogous to the theoretical models of Stommel (1948) and Munk & Carrier (1950). The apparatus and methodology used to test the linear theory, and to explore the non-linear flow régime, are described in §3. Finally, the results are discussed in §4, and they are compared in §5 with previous ocean circulation studies.

2. Linear theory

Consider slow steady flow in the sliced cylinder configuration. The governing equations are the non-dimensional linearized momentum and continuity equations for an incompressible homogeneous fluid of viscosity ν, written in a coordinate system rotating with the cylinder at an angular velocity Ω and scaled by the container's mean depth L and the lid's relative angular velocity $\epsilon\Omega$,

$$2\hat{k}\times\mathbf{q} = -\nabla p + E\nabla^2\mathbf{q}, \tag{1a}$$

$$\nabla.\mathbf{q} = 0. \tag{1b}$$

The Ekman number $E = \nu/\Omega L^2$ is assumed to be very small; and the boundary conditions on $\mathbf{q}$ are $\mathbf{q} = r\hat{\theta}$ at $z = 1$, $\mathbf{q} = 0$ at $r = a$, and $z = y\tan\alpha$. See figure 1 for x, y, z, where $x = r\cos\theta$, $y = r\sin\theta$.

Since our interest here is the α-dependent interior and vertical boundary-layer flow, we treat implicitly the Ekman layers developed on the top and bottom surfaces. The Ekman-layer suction is then expressed as a compatibility condition, on the interior and side-wall boundary-layer velocity components, just outside the Ekman layers:

$$\left.\begin{aligned} w &= \tfrac{1}{2}E^{\frac{1}{2}}\{2-\hat{k}.\nabla\times\mathbf{q}\}, \quad \text{at} \quad z = 1, \\ w &= \tan\alpha(\hat{\jmath}.\mathbf{q}) + \tfrac{1}{2}E^{\frac{1}{2}}\{\hat{k}.\nabla\times\mathbf{q} + O(\tan\alpha)\}, \quad \text{at} \quad z = y\tan\alpha. \end{aligned}\right\} \tag{2}$$

The term $\tan\alpha(\hat{\jmath}.\mathbf{q})$ represents the imposed vertical velocity of a fluid particle moving up the bottom slope. When terms of $O(E^{\frac{1}{2}}\tan\alpha)$ and higher are ignored for small α, the vertical velocity above the bottom Ekman layer consists of this orographic component plus the approximate Ekman-layer flux appropriate to a horizontal bottom. We shall see that, as α is increased from 0 to $O(1)$, the constraint imposed by the relative magnitude of the orographic component to the Ekman-layer suction governs the pattern of the complete flow.

Case 1: $0 < \tan\alpha \ll E^{\frac{1}{4}}$. The interior dynamics are geostrophic and are constrained by the Taylor–Proudman theorem for all α. The interior velocity components are independent of z to $O(E)$, and the fluid motion is columnar. If one matches vertical velocities in (2), one forms a steady vorticity equation,

$$\hat{k}.\nabla\times\mathbf{q} + \frac{\tan\alpha}{E^{\frac{1}{2}}}\hat{\jmath}.\mathbf{q} = 1, \tag{3}$$

which can be rewritten

$$\nabla^2 p + \frac{\tan\alpha}{E^{\frac{1}{2}}}\,p_x = 2, \tag{4}$$

using the pressure field as a stream function. Since the $O(1)$ interior radical flow must be zero at the boundary, the cylinder wall is a streamline and $p(a)$ constant. A particular solution of (4) is

$$p_p = \frac{2E^{\frac{1}{2}}}{\tan\alpha}x, \tag{5}$$

the flux into the top Ekman layer being balanced by the orographic component of a fluid column moving up the bottom slope. This is analogous to the Sverdrup (1947) balance in β plane dynamics. The homogeneous problem is reduced, by the substitution

$$p_h = f(x,y)\exp\left\{-\frac{x\tan\alpha}{2E^{\frac{1}{2}}}\right\}, \tag{6}$$

to a Helmholtz equation with modified Bessel function solutions. The general solution of the total problem is

$$p = \frac{a^2}{\Gamma}\left[x' + e^{-\Gamma x'}\left\{\sum_{m=0}^{\infty} I_m(\Gamma r')\,(C_{1m}e^{im\theta} + C_{2m}e^{-im\theta})\right\}\right], \tag{7}$$

where

$$\Gamma = \frac{a\tan\alpha}{2E^{\frac{1}{2}}}$$

and x' and r' are normalized by the scale radius a. The unknown Fourier coefficients are found by series evaluation of the boundary condition $p(a) = 0$, yielding for the pressure,

$$p = \frac{a^2}{\Gamma}\left[x' + e^{-\Gamma x'}\left\{\frac{I_1(\Gamma)}{I_0(\Gamma)} I_0(\Gamma r') + \sum_{m=1}^{\infty} \frac{I_{m+1}(\Gamma) + I_{m-1}(\Gamma)}{I_m(\Gamma)} I_m(\Gamma r') \cos m\theta\right\}\right]. \quad (8)$$

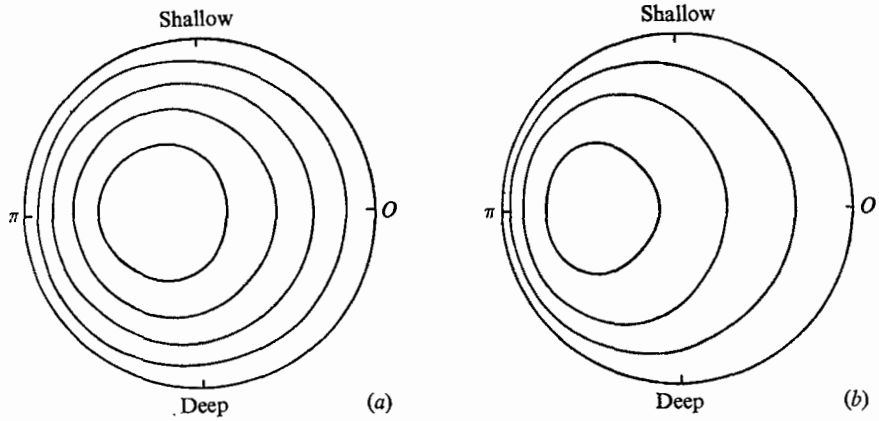

FIGURE 2. (a) $\Gamma = 1{\cdot}0$; (b) $\Gamma = 3{\cdot}0$.

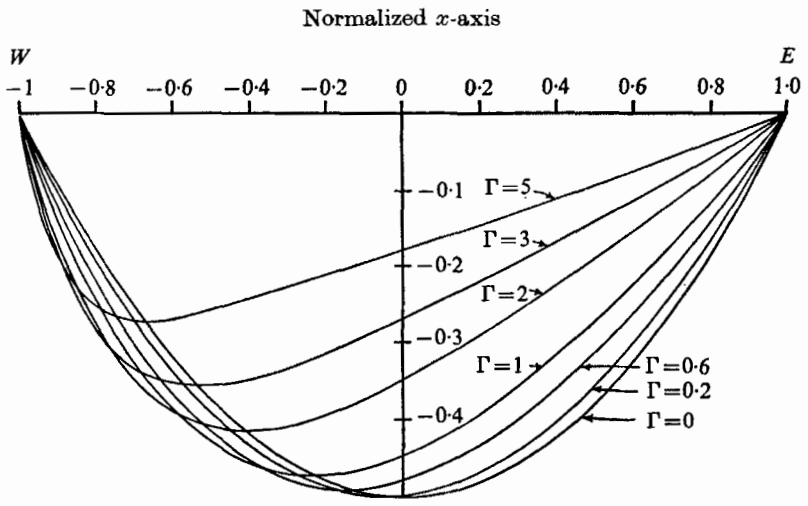

FIGURE 3

The series converges for finite $\tan\alpha$, and has been evaluated numerically. Two stream patterns are shown in figure 2, and the pressure along the x-axis shown in figure 3. The parameter Γ, proportional to the ratio of total depth change $r_0 \tan\alpha$ to Ekman-layer thickness $\sqrt{(\nu/\Omega)}$, expresses the importance of orographic uplift relative to Ekman-layer suction, and dictates the east–west asymmetry of the interior circulation.

The intense crowding of streamlines along the western boundary, for large values of Γ, indicates the development of a geostrophic western boundary layer,

in which vortex shrinking is balanced by Ekman-layer suction. The scale thickness of this layer is Γ^{-1} or $E^{\frac{1}{2}}/\tan\alpha$, while the boundary current azimuthal velocity is $O(1)$. The boundary flux matches the interior north–south flux, constrained by the bottom slope to be $O(E^{\frac{1}{2}}/\tan\alpha)$. These results are similar to Stommel (1948), since (4) is *identical* to the governing equation for the stream function examined by Stommel for two-dimensional β plane flow with 'bottom' friction.

As $\tan\alpha$ increases from $E^{\frac{1}{2}}$ toward $E^{\frac{1}{4}}$, this geostrophic layer forms and decreases in thickness toward the Stewartson $E^{\frac{1}{4}}$-layer scale, while the interior flow decreases toward $O(E^{\frac{1}{4}})$, the magnitude of the forced radial motion from the lowest-order geostrophic balance which a Stewartson $E^{\frac{1}{4}}$ layer can support. We shall see next that the $E^{\frac{1}{4}}$-layer structure is modified when $\tan\alpha$ approaches $E^{\frac{1}{4}}$.

Case 2: $E^{\frac{1}{4}} \sim \tan\alpha \ll 1$. We now examine the $E^{\frac{1}{4}}$ layer along the western boundary by letting $\tan\alpha = \Delta E^{\frac{1}{4}}$, with Δ at first assumed to be $O(1)$. The $E^{\frac{1}{4}}$-layer velocity and pressure fields are expanded in powers of $E^{\frac{1}{4}}$,

$$\mathbf{q} = \mathbf{q}_0 + E^{\frac{1}{4}}\mathbf{q}_1 + \ldots, \quad p = p_0 + E^{\frac{1}{4}}p_1 + \ldots, \tag{9}$$

with the stretched co-ordinate ζ, given by

$$\zeta = (a-r)E^{-\frac{1}{4}}.$$

The lowest-order Ekman-layer fluxes are given by (2) as

$$w_1 = v_{0\zeta}/2 \quad \text{at} \quad z = 1, \tag{10a}$$

$$w_1 = (-v_{0\zeta}/2) + \Delta\cos\theta v_0 \quad \text{at} \quad z = a\sin\theta\tan\alpha. \tag{10b}$$

As $\tan\alpha$ approaches $E^{\frac{1}{4}}$, the bottom slope is large enough to make the orographic component comparable to the Ekman-layer suction in the $E^{\frac{1}{4}}$ layer. In the vertically integrated continuity equation, the horizontal convergence is associated only with the ageostrophic part $\frac{1}{2}v_{0\zeta\zeta}$ of u_2 (as given by the $O(E^{\frac{1}{2}})$ azimuthal momentum equation), since the lower-order radial flow u_1 is entirely geostrophic. Thus, using (10),

$$v_{0\zeta\zeta\zeta} - 2v_{0\zeta} + 2\Delta\cos\theta v_0 = 0. \tag{11}$$

The lateral diffusion of vorticity from the side boundary is now balanced not only by Ekman-layer suction but also by orographic vortex stretching. For solutions of the form $A_i e^{\lambda_i\zeta}$, the λ_i's must satisfy the cubic

$$\lambda_i^3 - 2\lambda_i + 2\Delta\cos\theta = 0. \tag{12}$$

For $\Delta < (\frac{2}{3})^{\frac{3}{2}}$, i.e. $\tan\alpha < (\frac{2}{3})^{\frac{3}{2}}E^{\frac{1}{4}}$, for $\cos\theta < 0$, the two roots of (12), which give exponential decay into the interior along the western boundary, are real; this corresponds to a slight thickening of the normal θ-independent $E^{\frac{1}{4}}$ layer near $\theta = \pi$ and the thicker interior geostrophic boundary layer found in case 1. When the bottom slope reaches the critical value $\tan\alpha_c = (\frac{2}{3})^{\frac{3}{2}}E^{\frac{1}{4}}$, the interior and $E^{\frac{1}{4}}$ layers merge at $\theta = \pi$. For larger slopes, the two relevant roots of (12) become complex conjugates of the form

$$\lambda_\pm = -a + b\,e^{\pm\frac{2}{3}\pi i}, \tag{13}$$

with
$$a = \{\Delta|\cos\theta| - \sqrt{(\Delta^2\cos^2\theta - (\tfrac{2}{3})^3)}\}^{\frac{1}{3}},$$
$$b = \{\Delta|\cos\theta| + \sqrt{(\Delta^2\cos^2\theta - (\tfrac{2}{3})^3)}\}^{\frac{1}{3}},$$

along an arc centred about $\theta = \pi$. The transition points between real and complex roots occur at $\theta = \pi \pm \delta\theta$, where $\delta\theta = \cos^{-1}((\frac{2}{3})^{\frac{3}{2}}/\Delta)$.

For slopes much greater than the critical value, the end points of the arc rapidly approach $\frac{1}{2}\pi$ and $\frac{3}{2}\pi$, while the roots approach

$$\lambda_\pm = \sqrt[3]{(2\Delta|\cos\theta|)}\, e^{\pm\frac{2}{3}\pi}. \tag{14}$$

Thus, the Stewartson $E^{\frac{1}{4}}$ layer that exists for $\Delta \ll 1$ is modified by orographic stretching when $\Delta \sim 1$, and is replaced when $\Delta \gg 1$ by a thinner layer of scale

$$\frac{E^{\frac{1}{4}}}{\Delta^{\frac{1}{3}}} = \left(\frac{E}{\tan\alpha}\right)^{\frac{1}{3}}.$$

Here the lateral diffusion of vorticity is balanced primarily by orographic stretching rather than by Ekman-layer suction. Since the dynamics are otherwise the same as in a non-axisymmetric Stewartson $E^{\frac{1}{4}}$ layer (e.g. Barcilon 1967), this layer will be called a modified Stewartson $E^{\frac{1}{4}}$ or '$mE^{\frac{1}{4}}$' layer for $\Delta \gg 1$. The $O(E^{\frac{1}{4}})$ horizontal interior circulation is closed solely by this $mE^{\frac{1}{4}}$ layer, and an analysis similar to that of Pedlosky & Greenspan (1967) shows its azimuthal velocity to be to lowest order

$$v_0 = \frac{4\sqrt[3]{2}}{\sqrt{3}} \frac{a|\cos\theta|^{\frac{4}{3}}}{\Delta^{\frac{2}{3}}} \exp\{-\tfrac{1}{2}\tilde{\gamma}\zeta\} \sin\frac{\sqrt{3}\,\tilde{\gamma}\zeta}{2}, \tag{15}$$

where
$$\tilde{\gamma} = \sqrt[3]{(2\Delta|\cos\theta|)}.$$

This result, when rewritten in terms of α and E, is identical to the expression found by Pedlosky & Greenspan for the range $E^{\frac{1}{3}} < \tan\alpha \ll 1$ (their analysis of the western boundary layer as an $E^{\frac{1}{3}}$ layer implicitly assumes that $\tan\alpha > E^{\frac{1}{3}}$, in order to retain the orographic stretching to lowest order within the framework of the normal $E^{\frac{1}{3}}$-layer scaling). However, it is clear that the fundamental dynamics are essentially unchanged over the larger range of $E^{\frac{1}{4}} \ll \tan\alpha \ll 1$. As $\tan\alpha$ increases from $E^{\frac{1}{4}}$, the essentially hydrostatic $mE^{\frac{1}{4}}$ layer *shrinks* in thickness, to become the asymmetric $E^{\frac{1}{3}}$ layer indicated by the formalism of Pedlosky & Greenspan. The key to this thinning is of course the $mE^{\frac{1}{4}}$-layer vertical vorticity balance (11). For $\tan\alpha \ll E^{\frac{1}{4}}$, the lateral diffusion of vorticity from the side wall is balanced primarily by vortex stretching by both Ekman layers, and the interior flow is analogous to Stommel's model with 'bottom' friction. Increasing the bottom slope increases the orographic component of this stretching, until it dominates the Ekman-layer suction component. Any further increase in the orographic component caused by increasing the slope more must then be balanced by an enlarged lateral vorticity flux, i.e. a greater velocity shear and a thinner boundary layer. It is in this latter range of $E^{\frac{1}{4}} \ll \tan\alpha \ll 1$ that the interior and $mE^{\frac{1}{4}}$ flow is analogous to the Munk & Carrier (1950) model for two-dimensional flow on a β plane with lateral friction.

Secondary vertical circulation for $E^{\frac{1}{2}} < \tan\alpha \ll 1$†

While the interior Sverdrup circulation is closed to lowest order by the western $mE^{\frac{1}{4}}$ layer, the $O(E^{\frac{1}{2}})$ secondary vertical circulation is not. The vertical flux into the upper Ekman layer is to lowest order independent of θ, so the radial outflux from this layer is axisymmetric. For $\tan\alpha < E^{\frac{1}{2}}$ this flux is fed by the $E^{\frac{1}{3}}$ layer through the $E^{\frac{1}{4}}$ layer back into the bottom Ekman layer to close the circulation (Bisshopp 1966).

A moderate slope of $\tan\alpha > E^{\frac{1}{2}}$ constrains the outflux from the bottom Ekman layer to be $O(E/\tan\alpha) < E^{\frac{1}{2}}$, so the upper Ekman layer must instead feed the interior and western $mE^{\frac{1}{4}}$ layer directly *via* an axisymmetric $E^{\frac{1}{3}}$ layer.

By continuity, the net radial velocity of this $E^{\frac{1}{3}}$ layer is $u = -\frac{1}{2}aE^{\frac{1}{2}}$. Since the $mE^{\frac{1}{4}}$ layer exists along the western boundary only, the interior radial velocity must match the $E^{\frac{1}{3}}$-layer flux along the eastern boundary. Since the interior cross-contour velocity is fixed by the Sverdrup condition (5), the $E^{\frac{1}{3}}$-layer outflux must flow in the interior parallel to the depth contours, giving for the interior pressure, to $O(E^{\frac{1}{2}})$,

$$p = \frac{2E^{\frac{1}{2}}}{\tan\alpha}\left\{x - \sqrt{(a^2-y^2)} + \frac{\tan\alpha\, a^2}{2}\sin^{-1}\left(\frac{y}{a}\right)\right\}. \tag{16}$$

Matching the interior and the western half of the $E^{\frac{1}{3}}$ layer to the $mE^{\frac{1}{4}}$ layer yields for the complete boundary-layer azimuthal velocity to $O(E^{\frac{1}{6}})$

$$v = \epsilon\Omega L E^{\frac{1}{6}}\left\{\sum_{m=1}^{\infty}\frac{2a}{\sqrt{3}}\frac{(-1)^m\gamma_m}{m\pi}e^{-\frac{1}{2}\gamma_m\eta}\sin\frac{\sqrt{3}\,\gamma_m\eta}{2}\cos m\pi z\right.$$
$$\left. - |2\tan\alpha\cos\theta|^{\frac{1}{3}}\left\{\frac{4a\cos\theta}{\sqrt{3}\tan\alpha} + \frac{5a^2}{3\sqrt{3}}\sin 2\theta\right\}e^{-\frac{1}{2}\gamma\eta}\sin\frac{\sqrt{3}\,\gamma}{2}\eta\right\}, \tag{17}$$

where $$\eta = (a-r)E^{-\frac{1}{3}},$$

and $$\gamma_m = (2m\pi)^{\frac{1}{3}}, \quad \gamma = |2\tan\alpha\cos\theta|^{\frac{1}{3}}\{1 + \tfrac{1}{3}a\tan\alpha\cos\theta\}.$$

The vertical mass flux extracted from the interior by the upper Ekman layer is returned to the interior *via* the thinner axisymmetric $E^{\frac{1}{3}}$ layer. The radial outflux from this layer along the eastern side is carried *parallel* to the geostrophic contours into the ageostrophic western $mE^{\frac{1}{4}}$ layer, where it *converges* with the inner $E^{\frac{1}{3}}$-layer outflux along the western boundary. Because of this net convergence, the mass flux lost by the fluid column as it is carried through the interior region from the deep to the shallow end is *restored* as it returns to the deep end *via* the $mE^{\frac{1}{4}}$ layer. This convergence, along with the second-order influence of the bottom slope on the $mE^{\frac{1}{4}}$ boundary-layer thickness, distorts slightly the first-order, north–south symmetry. The position of the azimuthal velocity maximum is moved through an angle $\Delta\theta = \sin^{-1}(5a\tan\alpha/8)$ from the east–west axis toward the shallow end.

† The analysis for this case is a straightforward extension of the Pedlosky & Greenspan analysis to second order in $\tan\alpha$, and will be omitted, since it may be found in detail in Beardsley (1968). Restricting $\tan\alpha > E^{\frac{1}{2}}$ simply allows the Pedlosky & Greenspan formulation to be retained. It is thought, however, that the dynamics of closing the vertical circulation, outlined here, also apply over the wider range $E^{\frac{1}{4}} \ll \tan\alpha \ll 1$.

The possible discrepancy between (17) and the complete series solution is $O(E^{\frac{1}{2}})$, since the Ekman-layer contribution to vortex stretching in the $mE^{\frac{1}{4}}$ layer has been omitted. The experiments to be described next cover a range of E such that $0{\cdot}147 \leqslant E^{\frac{1}{2}} \leqslant 0{\cdot}198$, suggesting that the discrepancy may be appreciable. On the other hand, this theoretical analysis suggests that the western layer thickness dependence on E is valid over a wider range of $\tan\alpha \gg E^{\frac{1}{4}}$.

3. Experimental apparatus and methods

3.1. *Apparatus*

The fluid container consisted of a lucite cylinder ($25{\cdot}400 \pm 0{\cdot}005$ cm i.d.) capped at both ends by lucite plates (see figure 4). The sliced-cylinder geometry was formed by inserting a false top and bottom into the cylinder. Five lucite

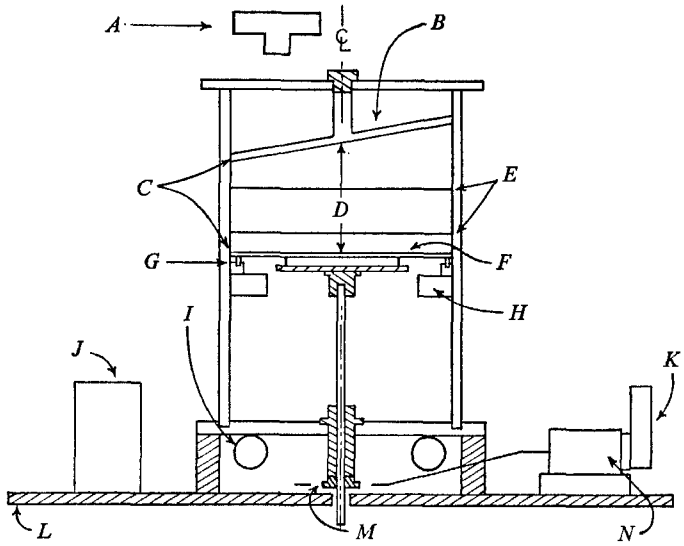

FIGURE 4. *A*, 35 mm camera; *B*, sloping 'bottom'; *C*, 0·025 cm clearance; *D*, 12·7 cm; *E*, 0·0025 cm diameter platinum wire; *F*, rotating glass disk; *G*, miniature ball bearing; *H*, expansion clamp; *I*, circular fluorescent lamp; *J*, sequence timer; *K*, clock motor; *L*, rotating table; *M*, worm gear; *N*, gear train.

bottoms were used with nominal angles of $\alpha \sim 6°$, 8°, 10°, 12° and 14°. The mean vertical separation between top and bottom L was $12{\cdot}75 \pm 0{\cdot}05$ cm. The geometry was inverted to facilitate construction and operation.

Two critical design features became apparent during preliminary experimentation. The lid driving the fluid must be flat and rotate in a fixed plane, and the angular velocities of both the driving lid and the turntable must be quite stable to ensure a constant stress or ϵ. A glass disk of diameter $24{\cdot}350 \pm 0{\cdot}002$ cm was used as the top driving plate. Its plane of rotation could be fixed by three supporting miniature ball bearings, since the glass disk was optically flat and its surfaces were parallel. The average separation between the side wall and the glass disk, and the side wall and false bottom, was 0·025 cm, about 45 % of the average Ekman-

layer scale thickness $LE^{\frac{1}{2}}$. No leakage from the sliced-cylinder section was observed.

To ensure stability the glass plate and turntable were driven by independent synchronous motors. The glass disk was connected by a gear train to a clock motor powered by an audio oscillator and amplifier system, so the relative angular velocity of the glass disk could be varied by adjusting either the oscillator frequency or the gear reduction ratio. The turntable was driven by a selected Graham variable-speed transmission. The relative angular velocity of the glass disk, dependent on the oscillator stability, was quite constant. The angular velocity of the turntable was less so, being limited mainly by the stability of line frequency. (A typical fractional standard deviation of the turntable's rotation period was $\sim 3 \times 10^{-4}$ (20 periods).)

3.2. *Flow visualization*

Velocity measurements were made in the interior and western boundary layer over a wide range of Rossby and Ekman numbers, using several flow visualization methods. The thymol blue pH indicator technique (Baker 1966) was used in the linear flow régime where relative velocities were smaller than 0·1 cm/s.

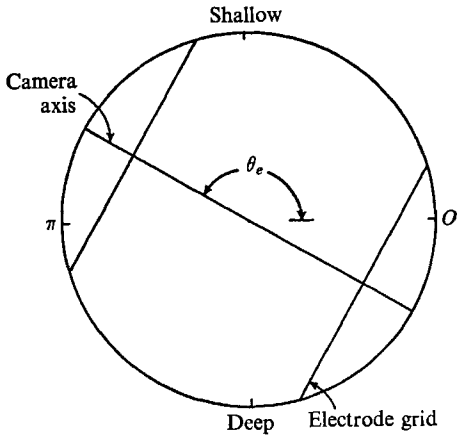

FIGURE 5

Two grids of 0·001 in. platinum–irridium wire (see figure 5) were stretched horizontally across the cylinder at $z/L = 0{\cdot}433$ and 0·826. The electrode orientation θ_e could be varied by simply twisting the sloping bottom insert. The cylinder was filled with a 0·1 N solution of thymol blue titrated to its basic end-point; applying a d.c. potential across the grids changed the pH around each wire, making the fluid at the positive electrode more basic and turning it deep blue. A sequence of these dye lines was photographed as they were swept off the electrode (see figure 6, plate 1). The horizontal distance between successive dye segments was measured along constant radius arcs and divided by the sequence interval to compute the observed velocity.

Velocities in the non-linear flow régime were greater than 0·1 cm/s, so other techniques were used. The horizontal structure was studied with streak photo-

graphy using an aluminium flake suspension illuminated from the side by a slit beam. A sequential starch–iodine dye method was used to study flow stability. Dye pulses formed in the western boundary layer were advected into the interior region, where they were photographed periodically. Repeatability of the pattern from photograph to photograph indicated steady flow, while temporal variation indicated unsteady flow.

The experimental procedure for all studies was similar. The minimum period allowed for spin-up was $2\pi/E^{\frac{1}{2}}\Omega$. The driving stress was then applied and, after waiting a similar period for transient decay, the flow observations were made.

4. Experimental results

The experimental program had two objectives: first, to compare the theoretical calculations with measurements of the interior cross-contour flow and of the western boundary-layer azimuthal velocity profile; secondly, to explore the non-linear response to large ϵ by studying visually the interior horizontal velocity structure.

4.1. *Interior flow*

The interior cross-contour velocity V_{CC} was measured at point P_I ($r/L = 0{\cdot}566$, $\theta_e = 0$, $z/L = 0{\cdot}826$) as a function of bottom slope and Rossby number. A second measurement was made 5·0 cm below P_I to check the predicted z dependence. The results (see figure 7 and table 1) indicate that the theoretical Sverdrup balance (5) accurately determines the two-dimensional cross-contour velocity component over the wide range of ϵ studied. Although precise measurements of the interior secondary horizontal flow, parallel to the depth contours, could not be made, the sign and order of magnitude of the flow were as predicted in (16).

4.2. *Western boundary-layer flow*

Velocity measurements were made to determine the dependence of the azimuthal velocity profile on E, α, θ and z. The dependency on E was studied near $\theta_e = \pi$ for $\alpha = 10°$, using 12 table rotation rates. A typical photograph is shown in figure 6, plate 1, and the measured profile is shown in figure 8. Two variables were compared: $\Delta r_{\max}$, the radial distance (cm) of the velocity maximum from the wall, and $V_{\max}/\epsilon\Omega L$, the scaled amplitude of the velocity maximum. The theoretical values computed from (17), and the observed values, were analyzed by the method of least squares (see figure 9 and table 2). While the amplitudes of $\Delta r_{\max}$ and $V_{\max}/\epsilon\Omega L$ are slightly less than predicted, the observed boundary-layer thickness is proportional to $E^{0{\cdot}33\pm0{\cdot}02}$, while the observed exponent of $0{\cdot}21 \pm 0{\cdot}02$ for $V_{\max}/\epsilon\Omega L$ is close to the predicted value of $\frac{1}{6}$.

Measurements of the maximum velocity made at four other azimuthal positions in the western boundary layer at fixed E and $\alpha = 10°$ correlated well with the theoretical envelope given by (17).

The largest discrepancy between theory and experiment occurred in the α and z dependencies. These were examined by measuring the velocity profile near $\theta_e = \pi$ at two depths for different α. The observed and theoretical relationships

are shown in figure 10 and table 2. The theoretical profile is some 8 % thicker at the lower position, while the velocity maximum is essentially the same at both levels. The observed profile was thinner than predicted at the upper level and thicker than predicted at the lower level. The observed flow was significantly slower, showing great vertical shear, and decreased inversely with $\tan\alpha$ at

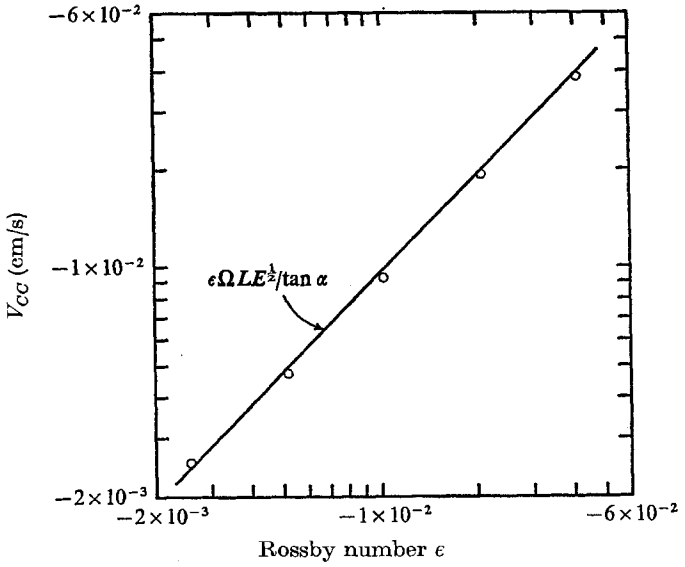

FIGURE 7

ϵ	$\tan\alpha$	z/L	†Predicted V_{CC}	†Observed V_{CC}	
−0·0026	0·111	0·826	3·89 ± 0·08	3·8 ± 0·1	Increasing $\tan\alpha$
−0·0026	0·144	0·826	3·02 ± 0·06	3·20 ± 0·2	
−0·0026	0·178	0·826	2·45 ± 0·05	2·53 ± 0·08	
−0·0026	0·178	0·434	2·43 ± 0·05	2·54 ± 0·12	Increasing $\lvert\epsilon\rvert$
−0·0052	0·178	0·826	4·9 ± 0·1	4·7 ± 0·2	
−0·0104	0·178	0·826	9·8 ± 0·2	9·3 ± 0·3	
−0·0208	0·178	0·826	19·6 ± 0·4	19·3 ± 0·6	
−0·0416	0·178	0·826	39·0 ± 0·8	38·0 ± 1·0	

† 1 velocity unit = 1×10^{-3} cm/s.

TABLE 1. Comparison of interior cross-contour velocity V_{CC} with theoretical values for different values of bottom slope, Rossby number, and vertical position. Experimental conditions: $\Omega = 3{\cdot}03$ rad/s, $E \simeq 1{\cdot}87\times10^{-5}$, $\theta_e = 0$

approximately half the predicted rate. The observed boundary layer was both slower and thicker at the bottom; the product $\Delta r_{\max} V_{\max}$, a transport indicator, agreed at both vertical positions. The observed deviations from theory are not presently understood.

4.3. *Horizontal structure in non-linear régime*

The non-linear flow régime showed a more marked north–south asymmetry in the western boundary layer as the driving stress was increased (see figure 11, plate 2). This asymmetry first appeared at $\alpha = 10°$, when $|\epsilon|$ was increased past

$E^{\frac{1}{2}}$. When $|\epsilon| \simeq 3E^{\frac{1}{2}}$, the western boundary layer partially closed upon itself to form a vortex in the north-west quadrant, and, when $|\epsilon| \simeq 6E^{\frac{1}{2}}$, this vortex shifted downstream to $\theta \simeq 130°$. An even larger stress increased the boundary-layer transport and the radial distance from vortex to side wall, but did not affect the azimuthal position of the vortex. Although the radial separation between

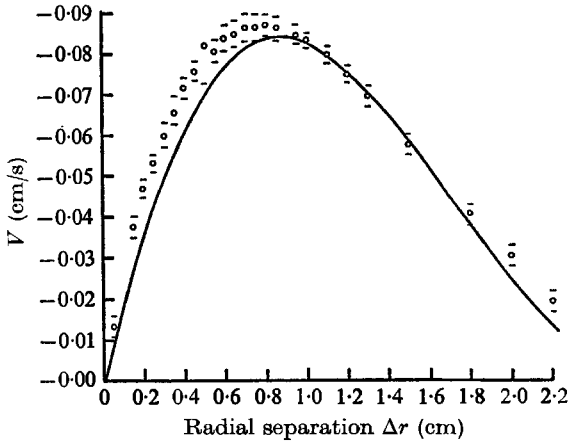

FIGURE 8

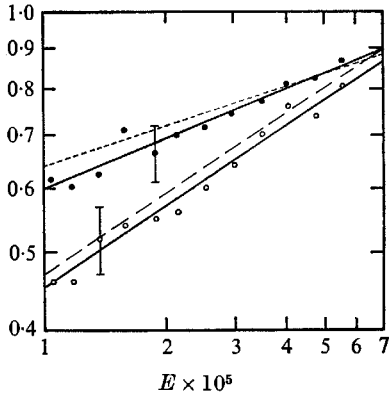

FIGURE 9. ●, $V_{max}/\epsilon\Omega L$: – – –, theory; ——, experiment. ○, Δr_{max} (cm): ——, theory; ——, experiment.

		Z/L	Theory	Experiment	Sample size
(*a*)	Δr_{max} (cm)	0·826	$e^{3\cdot08\pm0\cdot01}\,E^{0\cdot33}$	$e^{3\cdot03\pm0\cdot25}\,E^{0\cdot33\pm0\cdot02}$	(12)
	$V_{max}/\epsilon\Omega L$	0·826	$e^{1\cdot46\pm0\cdot01}\,E^{0\cdot167}$	$e^{1\cdot88\pm0\cdot15}\,E^{0\cdot21\pm0\cdot02}$	(12)
(*b*)	Δr_{max} (cm)	0·826	$e^{-1\cdot14\pm0\cdot09}\tan\alpha^{-0\cdot33\pm0\cdot05}$	$e^{-1\cdot05\pm0\cdot14}\tan\alpha^{-0\cdot23\pm0\cdot08}$	(13)
		0·434	$e^{-1\cdot06\pm0\cdot02}\tan\alpha^{-0\cdot32\pm0\cdot02}$	$e^{-0\cdot82\pm0\cdot20}\tan\alpha^{-0\cdot25\pm0\cdot11}$	(14)
	$V_{max}/\epsilon\Omega L$	0·826	$e^{-1\cdot37\pm0\cdot03}\tan\alpha^{-0\cdot81\pm0\cdot02}$	$e^{-1\cdot02\pm0\cdot22}\tan\alpha^{-0\cdot34\pm0\cdot12}$	(13)
		0·434	$e^{-1\cdot52\pm0\cdot01}\tan\alpha^{-0\cdot68\pm0\cdot01}$	$e^{-1\cdot26\pm0\cdot10}\tan\alpha^{-0\cdot35\pm0\cdot06}$	(13)

TABLE 2. Theoretical and observed dependence of Δr_{max} and $V_{max}/\epsilon\Omega L$ on Ekman number, bottom slope, and depth. Experimental condition: (*a*) $\alpha = 10°$, 1·03 rad/s $\leqslant \Omega \leqslant$ 5·43 rad/s, $\epsilon\Omega = -0\cdot0078$ rad/s; (*b*) $6° \leqslant \alpha \leqslant 14°$, $\Omega = 3\cdot03$ rad/s, $\epsilon = -0\cdot0026$, $1\cdot86\times10^{-5} \leqslant E \leqslant 2\cdot08\times10^{-5}$

vortex and wall increased with decreasing α at a given value of ϵ, the same terminal angular position of the vortex was observed to $\pm 3°$ for all α. Measurements at $z/L = 0\cdot725$ and 0·256 indicated that the vortex axis was aligned with the Ω axis to $\pm 2°$.

Fluid leaving the western boundary layer entered the interior through a transition region, where the extra inertia and vorticity acquired by non-linear processes in the western boundary layer were lost. This transition region thickened with increasing $|\epsilon|$ until topographic Rossby waves appeared (see figure 11, plate 2). The streamline pattern was stationary; only propagating waves with phase

speed equal and opposite the boundary-layer eastward outflux were present. Data indicate the stream pattern was two-dimensional, with wavelength proportional to $\sqrt{\epsilon}$ and $\tan\alpha^{-\delta}$ with $0{\cdot}5 < \delta < 1$ (a half wavelength was defined as the distance between two successive points where $\mathbf{q}.\hat{j} = 0$ along the depth contour through the boundary-layer vortex).

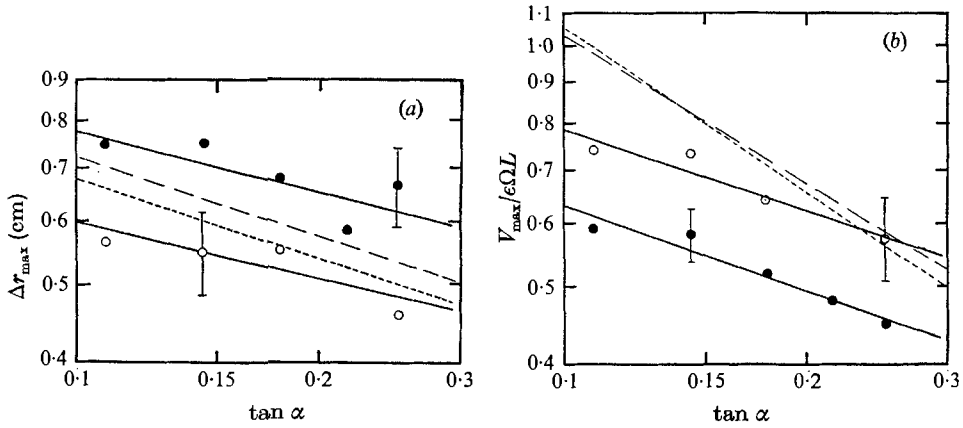

FIGURE 10. (*a*) ●, $Z/L = 0{\cdot}43$: ——, experiment; – – – theory. ○, $Z/L = 0{\cdot}83$: – – – –, theory; ——, experiment. (*b*) ○, $Z/L = 0{\cdot}83$: — — —, theory; ——, experiment. ●, $Z/L = 0{\cdot}43$: – – – –, theory; ——, experiment.

4.4. *Onset of instability*

The steady flow became unstable when a critical value of ϵ was reached. A small oscillation of the boundary-layer vortex appeared and a secondary vortex, forming periodically in the transition region, moved through the region as it decayed (see figure 12, plate 3). This vortex was two-dimensional, to the extent that its centre followed similar paths at $z/L = 0{\cdot}256$ and $0{\cdot}724$.

Reynolds numbers based on the western boundary layer and interior flows are equivalent, since their horizontal transports are approximately equal by continuity. The western boundary-layer Reynolds number is then

$$R_{WBL} = R_I = \left|\frac{V_{CC}L}{\nu}\right| = \frac{|\epsilon|}{\tan\alpha\, E^{\frac{1}{2}}}.$$

Two sets of data were used to calculate the dependence of R^c_{WBL} (the critical value of R_{WBL} governing onset of instability) on the parameters E, ϵ, α. When E and ϵ were varied, and $\alpha = 10°$ (see figure 13), R^c_{WBL} was a slowly increasing linear function of E. When E was held approximately constant at 2×10^{-5} and ϵ and α varied (figure 14), R^c_{WBL} was proportional to $(\tan\alpha)^{-1}$. The critical parameter governing onset of instability is then $R_E = |\epsilon|E^{-\frac{1}{2}}$, a Reynolds number based on the vertical flux into the top Ekman layer and independent of α. The stability curve is

$$R^c_E = \tan\alpha\, R^c_{WBL} = 11{\cdot}3 \pm 0{\cdot}2 + (1{\cdot}26 \pm 0{\cdot}05) \times 10^5 E.$$

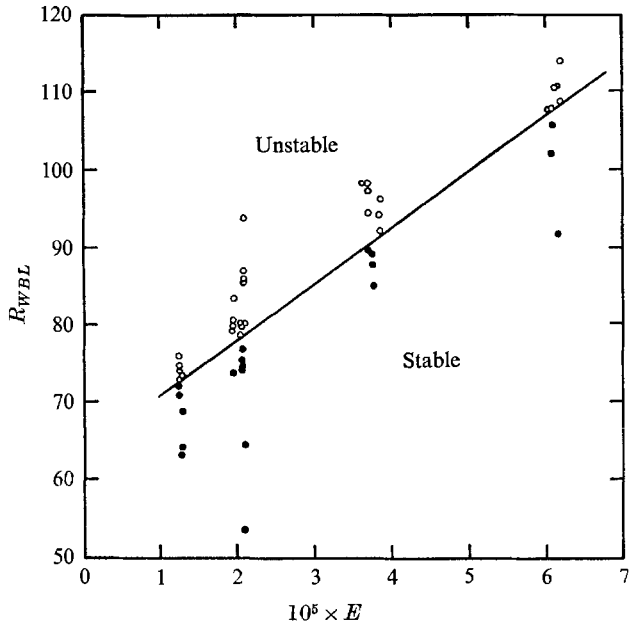

FIGURE 13

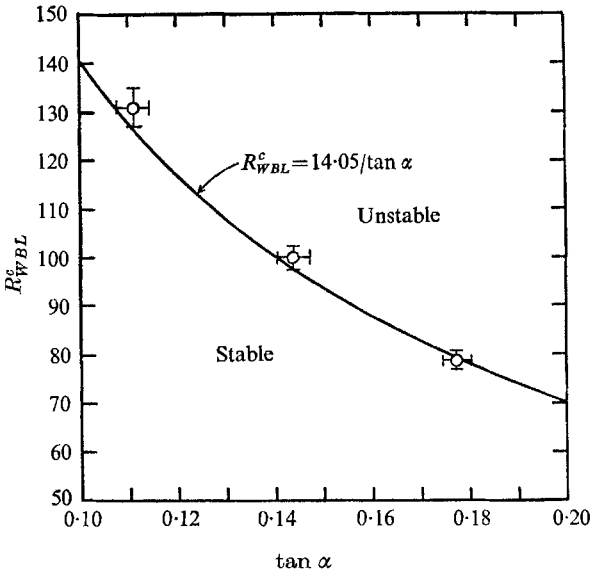

FIGURE 14

The observed oscillation period T, i.e. the time between formations of the secondary vortex, was also independent of α (see figure 15).†

From these results, some discussion of the instability mechanism is possible. The two-dimensionality of the secondary vortex does not isolate the source of the instability in the western boundary layer or transition region. The independence from α of T and R_E^c suggests that the Ekman or Stewartson $E^{\frac{1}{3}}$ layers may initiate the instability rather than a breaking-down of the steady topographic wave mechanism. The Ekman-layer instabilities discussed by Lilly (1966) and others, however, occur at values of $R_E \geqslant O(50)$, and are of relatively high frequency, with typical periods of less than one rotational day.

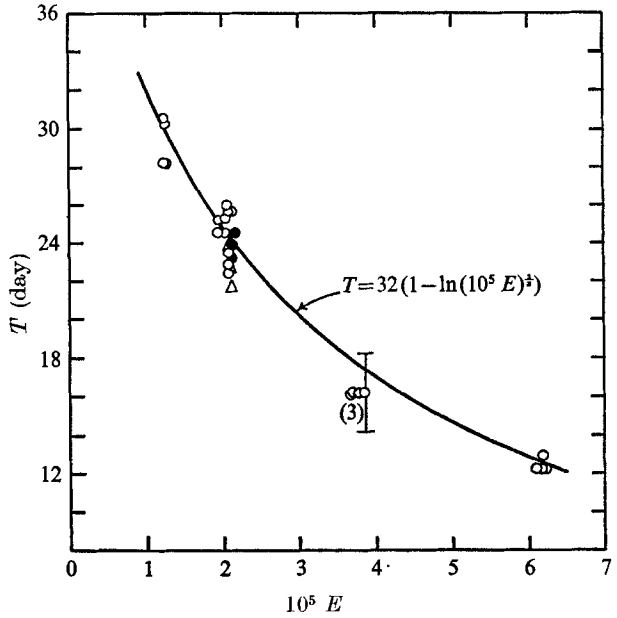

FIGURE 15

5. Comparison with previous β-plane models

Pedlosky & Greenspan (1967) pointed out the striking similarity of the theoretical flow in the sliced cylinder model to certain early linear β plane solutions of the wind-driven ocean circulation problem (e.g. Munk & Carrier 1950, for $\tan\alpha \gg E^{\frac{1}{4}}$). When they were compared with actual values of Gulf Stream width and transport, the computed eddy viscosity values were so unrealistically large that more recent studies have concentrated on the non-linear dynamics that affect the western boundary-layer vorticity balance. The β plane studies of

† The initial experiments reported by Pedlosky & Greenspan were carried out in a smaller basin (L = 13·4 cm, r_0 = 9·6 cm) of different aspect ratio (r_0/L = 0·71). The photograph (Pedlosky & Greenspan, figure 7) showing the periodic 'meanders' forming in the boundary-layer transition region was taken at $\alpha = 20°$, $\epsilon = -0{\cdot}10$, $E = 3{\cdot}2 \times 10^{-6}$, giving a value of R_E = 17·8, well above the critical value found here, R_E^c = 15·4.

Fofonoff (1954), Charney (1955), Carrier & Robinson (1962), and others, all indicated the purely inertial character of downstream intensification of the western boundary layer which is shown here as ϵ is increased.

More recently, Ilyin & Kamenkovich (1963) and Moore (1963) have discussed how an inertial western boundary-layer flux might be closed back into the interior in the northern half of the basin by imposing damped Rossby waves on the eastward zonal outflux from the boundary layer. The more exact numerical study by Bryan (1963) illustrated this mechanism. Here, analogous stationary topographic waves close the horizontal circulation and help stabilize the western boundary layer. With westward phase velocity, but eastward group velocity, they can carry out of the western boundary-layer region *via* the wave mechanism a larger flux of vorticity than can be simply convected.

The sliced-cylinder flow and Bryan's β plane model may be further compared, since both obey similar vertical vorticity equations to lowest order when $E^{\frac{1}{4}} \ll \tan\alpha \ll 1$. Bryan's unstable case at $R_I = 100$ is apparently similar to the instability observed here. A non-linear vorticity analogue to the sliced-cylinder model is currently being studied, to see if a two-dimensional model can reproduce the observed instability and its dependence on the external parameters.

I wish to thank H. Greenspan, R. Hide, M. McIntyre, J. Pedlosky, W. Seigmann and members of the M.I.T. Geophysical Fluid Dynamics Laboratory for many helpful discussions and suggestions. This research was supported by N.S.F. (Grant GP 5053), O.N.R. (Grant NONR-1841(74)), and a Hertz Foundation Fellowship.

REFERENCES

BAKER, D. J. 1966 A technique for the precise measurement of small fluid velocities. *J. Fluid Mech.* **26**, 573.

BARCILON, V. 1967 On the motion due to sources and sinks distributed along the vertical boundary of a rotating fluid. *J. Fluid Mech.* **27**, 551.

BEARDSLEY, R. C. 1968 Ph.D. Thesis, M.I.T.

BISSHOPP, F. E. 1966 Linearized flow in rotating systems. *Technical Report*, no. 2, Brown University.

BRYAN, K. 1963 A numerical investigation of a non-linear model of a wind-driven ocean. *J. Atmos. Sci.* **20**, 594.

CARRIER, G. F. & ROBINSON, A. R. 1962 On the theory of the wind-driven ocean circulation. *J. Fluid Mech.* **12**, 49.

CHARNEY, J. 1955 The Gulf Stream as an inertial boundary layer. *Proc. natn. Acad. Sci. U.S.A.* **41**, 731.

FOFONOFF, N. P. 1954 Steady flow in a frictionless homogeneous ocean. *J. Mar. Res.* **13**, 254.

GREENSPAN, H. P. 1965 On the general theory of contained rotating fluid motion. *J. Fluid Mech.* **22**, 449.

ILYIN, A. N. & KAMENKOVICH, V. M. 1963 On the influence of friction on ocean currents. *Dokl. Akad. Nauk SSSR*, **150**, 1274.

LILLY, D. K. 1966 On the instability of Ekman boundary flow. *J. Atmos. Sci.* **23**, 481.

MOORE, D. W. 1963 Rossby waves in ocean circulation. *Deep-Sea Res.* **10**, 735.

MUNK, W. H. & CARRIER, G. F. 1950 The wind-driven circulation in ocean basins of various shapes. *Tellus*, **2**, 158.

PEDLOSKY, J. & GREENSPAN, H. P. 1967 A simple laboratory model for the oceanic circulation. *J. Fluid Mech.* **27**, 291.

STOMMEL, H. 1948 The westward intensification of wind-driven ocean currents. *Trans. Am. Geophys. Union*, **29**, 202.

SVERDRUP, H. 1947 Wind-driven currents in a baroclinic ocean. *Proc. natn. Acad. Sci. U.S.A.* **33**, 318.

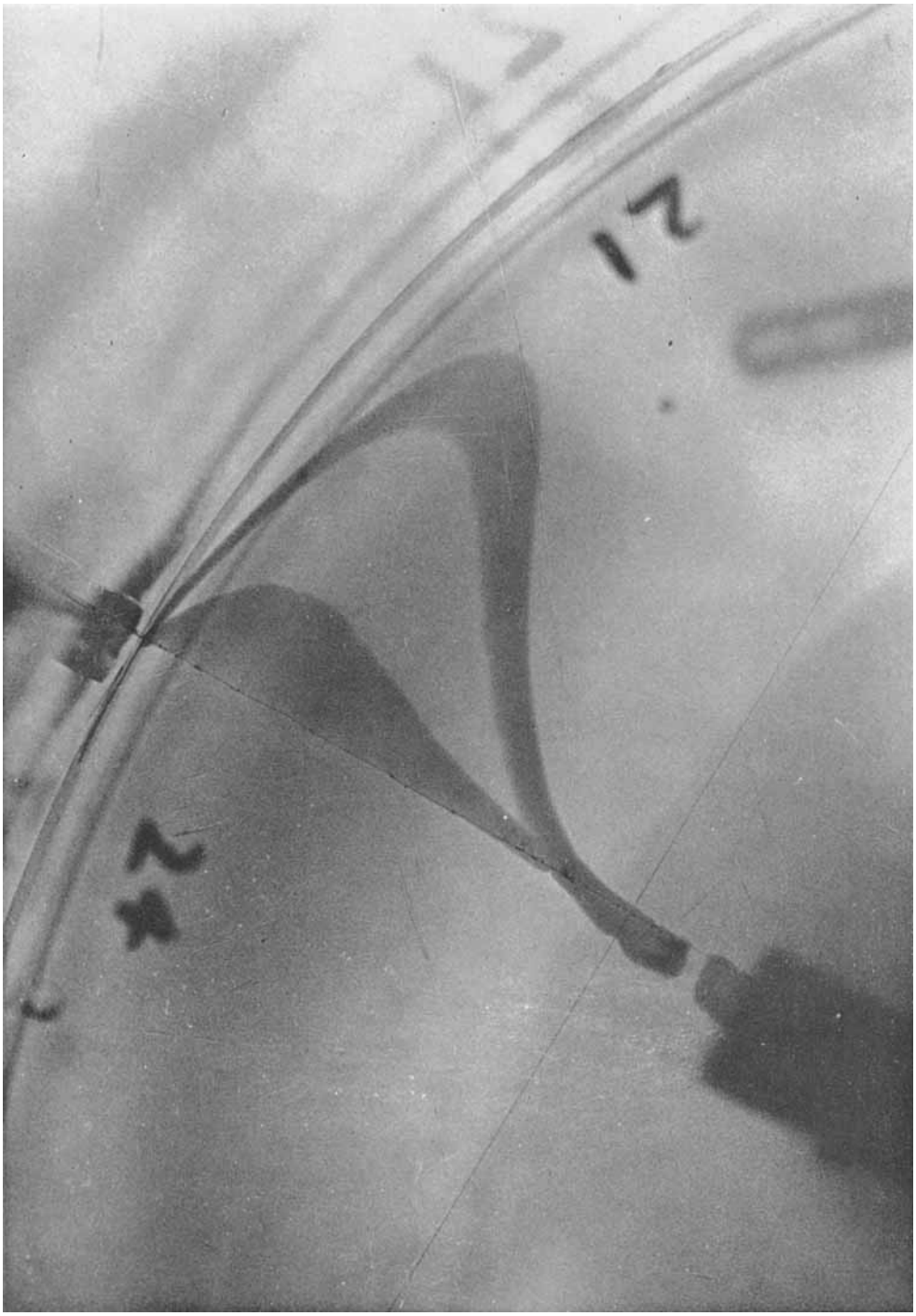

FIGURE 6. Azimuthal velocity in western boundary layer for 10° sloping bottom. Experimental conditions correspond to figure 7. Interval between dye pulses is 25 s. Radial distance along electrode between side wall and cross-wire is 3·72 cm.

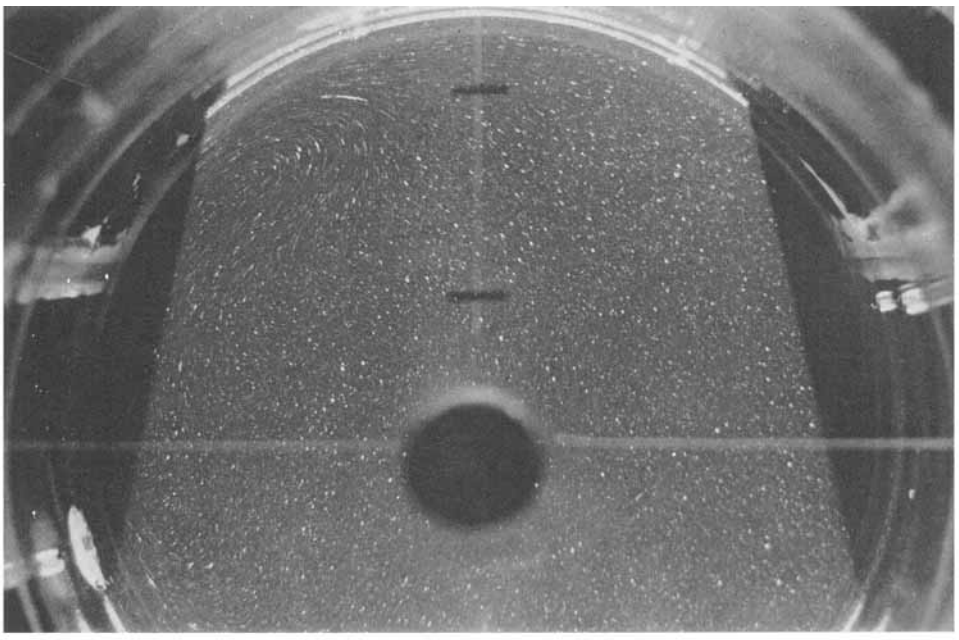

(*a*)

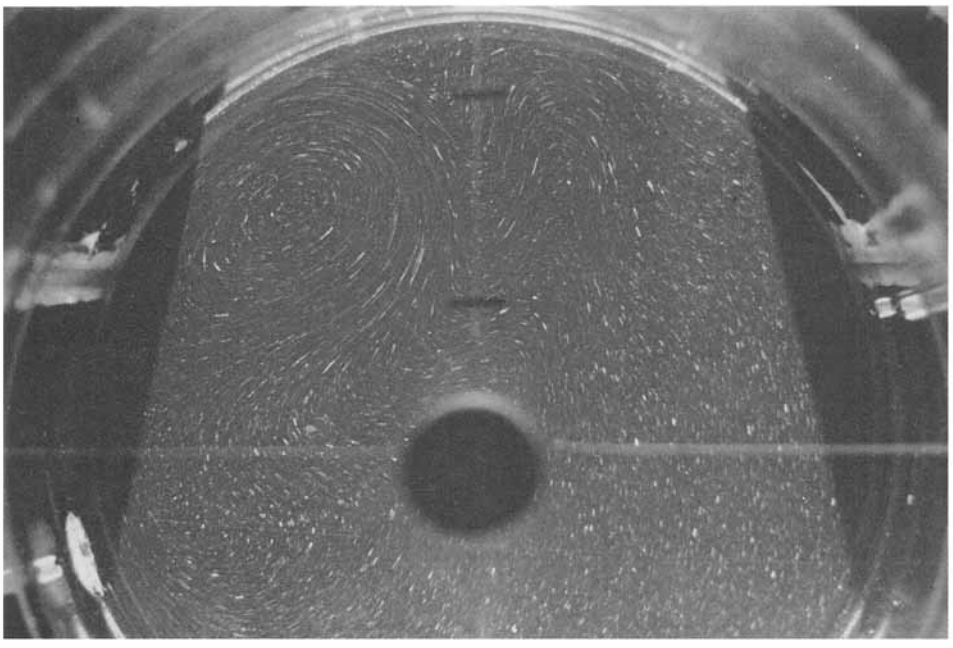

(*b*)

FIGURE 11. Horizontal velocity structure in northern half of basin for 10° sloping bottom. Experimental conditons: $\Omega = 3{\cdot}03$ rad/s, $E = 2{\cdot}03 \times 10^{-5}$, $Z/L = 0{\cdot}62$. (*a*) Exposure time, 4·88 s; $\epsilon = -0{\cdot}0190$; $|\epsilon|/E^{\frac{1}{2}} = 4{\cdot}21$. (*b*) Exposure time, 3·25 s; $\epsilon = -0{\cdot}0596$; $|\epsilon|/E^{\frac{1}{2}} = 13{\cdot}21$.

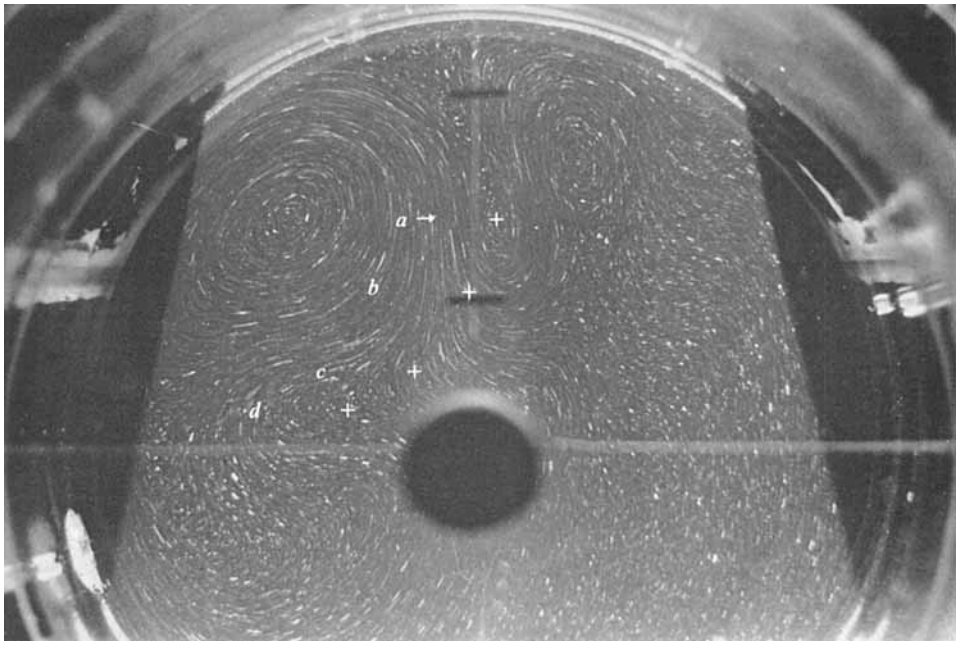

FIGURE 12. Horizontal velocity structure for unstable mode in northern half of basin for 10° sloping bottom. Letters indicate position of secondary vortex at the time 6·4 days (*b*), 12·9 days (*c*) and 19·3 days (*d*) after formation at *a*. Formation period of secondary vortex was 23·5 days (1 day = $2\pi/\Omega$ s). Experimental conditions: $\Omega = 3{\cdot}03$ rad/s, $E = 2{\cdot}04 \times 10^{-5}$, $z/L = 0{\cdot}62$, exposure time = 3·25 s.